Investigation of Dynamic Adsorption and Desorption of Polymer Nanogel in Porous Media through Microfluidics

Junchen Liu[1], **Fuqiao Bai**[2], **Abdulaziz A. Almakimi**[1], **Mingzhen Wei**[1], **Xiaoming He**[3],
Ibnelwaleed A. Hussein[4], **and Baojun Bai**[1]*

[1]Department of Geosciences and Geological and Petroleum Engineering, Missouri University of Science and Technology
[2]Hildebrand Department of Petroleum and Geosystems Engineering, The University of Texas at Austin
[3]Department of Mathematics and Statistics, Missouri University of Science and Technology
[4]College of Engineering, Qatar University

Summary

Understanding the transport and retention of elastic nanogel and microgel particles in porous media has been a significant research subject for decades, essential to the application of enhanced oil recovery (EOR). However, a lack of dynamic adsorption and desorption studies, in which the kinetics in porous media are seldom investigated, hinders the design and application of polymer nanogel in underground porous media. In this work, we visualized and quantified the transport and dynamic adsorption of polymer nanogel in 3D glass micromodels that were manufactured by packing glass beads in capillaries. Calibrating the linearity of fluorescence intensity to concentration, we calculated the adsorption kinetics at concentrations of 0.1 wt%, 0.2 wt%, and 0.3 wt% and flow rates of 0.01 mL/h, 0.02 mL/h, and 0.03 mL/h. In addition to time, concentration, and flow rate, the experimental results showed that dynamic adsorption is also a function of transport distance, which is due to the different adsorption abilities of particles. We also found that the uneven adsorption distribution can be attenuated by decreasing nanogel concentration or increasing flow rate. The work provides a new method to obtain adsorption and desorption kinetics and adsorption profile of submicron particles in porous media at flowing conditions through microfluidics.

Introduction

Transport and retention of submicron particles in porous media present pervasive, significant, and challenging issues in various environmental, medical, agricultural, and industrial domains (Zhang et al. 2021a; Chan and Almutairi 2016; Sivaram et al. 2015; Wu et al. 2023). In the oil and gas industry, polymer nanogels (also named micro/nanospheres), which are crosslinked polymers with 3D networks, have also attracted a lot of interest for EOR (Hou et al. 2020; Wu et al. 2021; Tian et al. 2012; Liu et al. 2022; Almohsin et al. 2014; El-Diasty and Aly 2015). It is believed that the deformable and size-controllable nanogels can enhance oil recovery through disjoining pressure (Liang et al. 2019; Zhou et al. 2023; Chen et al. 2022), interfacial tension reduction (Geng et al. 2020; Han et al. 2020; Ding et al. 2020), wettability alteration (Wang et al. 2021; Geng et al. 2018), and/or sweep efficiency improvement (Lenchenkov 2017; Geng et al. 2018; Wang et al. 2021; Zhou et al. 2023) for in-depth fluid diversion in heterogeneous reservoirs. Besides, nanogels not only have designed particle size for optimal accommodation within the target reservoir, thereby enhancing injectivity (Jia et al. 2014; He et al. 2021; Qiu et al. 2017), but also offer the convenience of direct injection into reservoirs after blending with injection water, resulting in reduced labor costs and injection processes (Liu et al. 2012; Yao et al. 2012, 2015, 2016). Despite these advantages, there are still many debates about applying nanogels in oil fields, with a key concern about whether enough particles can be delivered to target zones after long-distance retention onto the formation rocks (Liu et al. 2022; Seright and Liang 1995).

Some researchers have conducted experimental studies regarding the retention of polymer nanogels during transport in porous media, which can be divided into physical plugging and adsorption studies. Physical plugging is the main retention mechanism when particle size is close to or larger than pore throat size. Theoretically, it should take place when particles reach the target zones after a long distance of transport and swelling. Consisting of mechanical trapping and log-jamming, physical plugging is usually investigated by calculating plugging efficiencies and residual resistance factors in coreflooding tests and filtration tests (Sun et al. 2017; El-Diasty and Aly 2015; Yuan et al. 2021; Shi and Yue 2020; Dai et al. 2017; Han et al. 2019). These experiments illustrate the transport and retention of particles in porous media (cores and sandpack) by showing the distribution of plugging efficiencies, resistance factors, and residual resistance factors along the injection direction. It should be noted that the amount of retained particles in porous media cannot be directly determined by plugging efficiencies and residual resistance factors, even when scanning electron microscope photos are taken to show the position of retained particles in the cores (Chen et al. 2020a; Hua et al. 2014; Li et al. 2019). Microfluidic models have also been applied to observe and model the physical plugging in recent years (Yao et al. 2014, 2016, 2020; Li et al. 2020, 2021a; Wu et al. 2022; Chen et al. 2020b; Sun et al. 2018, 2020). When the particle size is much smaller than the pore size of reservoirs, adsorption is the main retention mechanism, especially for particles during the transport stage. In fact, adsorption happens in both transport and blocking stages and it is found that many nanogels showed very low resistance factors and plugging efficiencies in coreflooding tests, which indicates that adsorption plays a more important role than physical plugging in their experiments (Yu et al. 2016; Li et al. 2021b; Ding 2020; Almohsin et al. 2014).

Although investigation of nanogel adsorption is necessary to estimate the amount of particles that can be delivered and retained in the target zones, the related research is limited in the oil and gas industry because many researchers only pay attention to the physical plugging of large particles. Currently, there are only a small number of adsorption experiments, and they can be classified as static adsorption

---

*Corresponding author; email: baib@mst.edu

Original SPE manuscript received for review 11 March 2024. Revised manuscript received for review 9 October 2024. Paper (SPE 223943) peer approved 31 October 2024. Supplementary materials are available in support of this paper and have been published online under Supplementary Data at https://doi.org/10.2118/223943-PA. SPE is not responsible for the content or functionality of supplementary materials supplied by the authors.

or dynamic adsorption, depending on whether the experiments are conducted under flowing conditions. In terms of static adsorption, the porous media (rock or sand) is immersed in the particle dispersion, and the adsorption amount is calculated based on the change in particle concentration. Geng et al. conducted static adsorption of three different nanogels on sandstone using an ultravilet-visible (UV-vis) spectrophotometer (Lambert-Beer Law) and they found the multilayer adsorption of nanogel on the sandstone surface was dominated by electrostatic interactions (Geng et al. 2018). In addition to static adsorption, there are more studies of dynamic adsorption because the flowing condition is closer to the real reservoir environment. The investigation of dynamic adsorption can be divided into three types. The first one is the calculation of adsorption amount by utilizing mobility reduction and layer thickness (Chauveteau et al. 2004; Feng et al. 2003; Rousseau et al. 2005; Chauveteau et al. 2003; Cozic et al. 2008). However, the mobility reduction cannot distinguish between adsorption and physical plugging. The second method uses a segmented sandpack that can be dismantled into several sections. Using a UV-vis spectrophotometer, the component of each part can be analyzed after particle injection, and the concentration in each part of the sandpack is determined, as well as the particle adsorption amount (Li 2016). In addition to the UV-vis spectrophotometer, many researchers in environmental science measured the weight difference between the clean sand and dirty sand (the sand after retention) to show the retention profile (Xu et al. 2006; Ma et al. 2018). Although the specially designed sandpack can show the retention profile of particles, it is not able to distinguish adsorption and physical plugging in it. The researchers can only show a final retention amount instead of adsorption kinetics. Adsorption kinetics is essential for predicting nanogel behavior in porous media, as it provides real-time data on the rate of particle adsorption and desorption. This enables researchers to distinguish between immediate and long-term adsorption mechanisms, offering a more detailed understanding of the adsorption process. What is more, the experimental errors of the weight differences are not negligible for a very small amount of retention. The third method, which is also the most used one, analyzes the concentration history of effluents (breakthrough curves) from coreflooding by UV-vis or total organic analyzer (Lenchenkov 2017; Geng et al. 2018; Ding et al. 2020). It is effective in determining the total adsorption amount using the third method. However, it also fails to provide real-time adsorption kinetics.

In addition to the limited adsorption study, the particle concentration profiles in these experiments cannot be visually presented or thoroughly investigated. The opaqueness of cores presents a significant challenge in conventional coreflooding tests, where the primary obstacle lies in quantifying the amount of nanogel not bound to the grains of porous media but capable of unrestricted flow within the pore space (suspended particles). The application of advanced imaging techniques, such as microcomputed tomography (μCT), nuclear magnetic resonance spectroscopy (NMR), X-ray and focused ion beam scanning electron microscopy (FIB), are hindered by their prohibitive cost and time-consuming nature (Gaol et al. 2020). What is more, the techniques are not able to detect nanogel because its particle size is smaller than their resolutions. Recently, it has been reported that magnetic resonance imaging can be used to observe nanocolloids transport in porous media (Lehoux et al. 2017). However, the nanocolloids need to have iron oxide cores and the concentration should be very high to be detected. To obtain the adsorption kinetics, some researchers assume that the particle concentration in slim tubes varies linearly between the inlet and the outlet, but the assumption is not validated in porous media (Zhang et al. 2015). In summary, the current techniques fail to visualize the transport or quantify the adsorption/desorption kinetics due to the challenges of observation, time consumption, accuracy, and resolution **(Table 1)**.

	Classification		Methods	Challenges
Retention	Physical plugging	Log-jamming Mechanical trapping	Fr and Frr (Sun et al. 2017; El-Diasty and Aly 2015; Yuan et al. 2021; Shi and Yue 2020; Dai et al. 2017; Han et al. 2019; Almohsin et al. 2014); Microfluidics (Yao et al. 2014, 2020; Li et al. 2020; Sun et al. 2020)	Does not determine the amount of retained particles
	Adsorption	Static adsorption	UV-vis (Geng et al. 2018)	Not flowing condition
		Dynamic adsorption	Mobility reduction (Chauveteau et al. 2003, 2004; Feng et al. 2003; Rousseau et al. 2005)	Does not distinguish adsorption and physical plugging, no kinetics
			Segmented sandpack (Li 2016)	Does not distinguish adsorption and physical plugging, no kinetics
			Breakthrough curves (Cao et al. 2020; Lenchenkov 2017; Geng et al. 2018; Ding et al. 2020)	Does not distinguish adsorption and physical plugging, no kinetics
			Weight difference (Xu et al. 2006; Ma et al. 2018)	Experimental errors, no kinetics
			Nuclear magnetic resonance (Lehoux et al. 2017)	Time, cost, and resolution

Fr = resistance factor; Frr = residual resistance factor.

Table 1—Summary of retention experiments.

In this work, we established a new method to investigate nanogel transport and adsorption through microfluidics. First, we synthesized fluorescent nanogel by suspension polymerization and we fabricated 3D glass microfluidic models by sintering glass beads in quartz capillaries. After obtaining the linear relationship between nanogel concentration and fluorescence intensity, we conducted the nanogel injection in the 3D micromodels and recorded the fluorescence intensity and injection pressure in real time using confocal microscopy. Then, the nanogel concentration distribution was shown and adsorption/desorption kinetics were determined based on the linear relationship above and the mass conservation principle. Finally, we investigated the factors influencing dynamic adsorption and its distribution.

Materials and Methods

Materials. Acrylamide, N,N'-methylene bis(acrylamide) (MBAA, 99%), polyethylene glycol sorbitan monostearate (Tween 60), and ammonium persulfate (98%) were purchased from Sigma-Aldrich (St. Louis, Missouri, USA). Acryloxyethyl thiocarbamoyl Rhodamine

B (95–100%) was purchased from Polysciences, Inc. N-decane (99%) and sorbitan monooleate (Span 80) were purchased from Alfa Aesar. Ethanol (reagent grade) was purchased from Carolina Biological Supply Company. Deionized water was prepared in the laboratory using an ultrapure water system. Borosilicate glass spheres (GL0179B6/75, 200 mesh, wt% 75–85% Silica, wt% 12–16% boron oxide, wt% 2–6% sodium oxide, and wt% 2–5% aluminum oxide) were purchased from Mo-Sci, LLC. Squared quartz capillary tubes (ST0.5) were purchased from Technical Glass Products, Inc. Flexible fused silica capillary tubes (inside diameter = 200 µm) were purchased from Molex, LLC. Microscope slides were purchased from AmScope. The epoxy adhesive was purchased from Devcon. Immersion aqueous liquid [ρ = 1920 kg/m^3; μ = 7.68 cp; refractive index (RI) = 1.47] was purchased from Cargille Labs. Alexa Fluor 647 carboxylic acid (A33084) was purchased from Thermo Fisher Scientific Inc.

Nanogel Synthesis. The fluorescent nanogel was synthesized by inverse suspension polymerization of which the procedures were similar to our previous study (Zhang et al. 2021b). The detailed synthesis steps are shown in the Supplementary Material.

Micromodel and Fluid Preparation. The 3D transparent micromodels were fabricated by densely packing the borosilicate glass beads (75 µm) in the squared quartz capillary tubes (length = 3 cm; inner width = 0.5 mm; inner height = 0.5 mm; thickness = 0.25 mm). To maintain a stable pore structure, the glass beads and quartz capillary tubes were sintered together by heating the micromodels in a Muffle furnace at 850°C for 100 seconds. The porosity and permeability average throat size were 40% and 6500 mD. (Porosity measurements are shown in **Fig. S-1** of the Supplementary Material.) After that, the quartz capillary tubes with packed glass beads were placed on microscope slides, and two flexible fused silica capillary tubes (inside diameter = 200 µm) were connected with the model as the inlet and the outlet. (The glass beads packed section, the porous media between two silica capillary tubes, is 2.5 cm long.) Finally, the joints of micromodels and silica capillary tubes were fixed together by epoxy adhesive as shown in **Figs. 1a and 1b**.

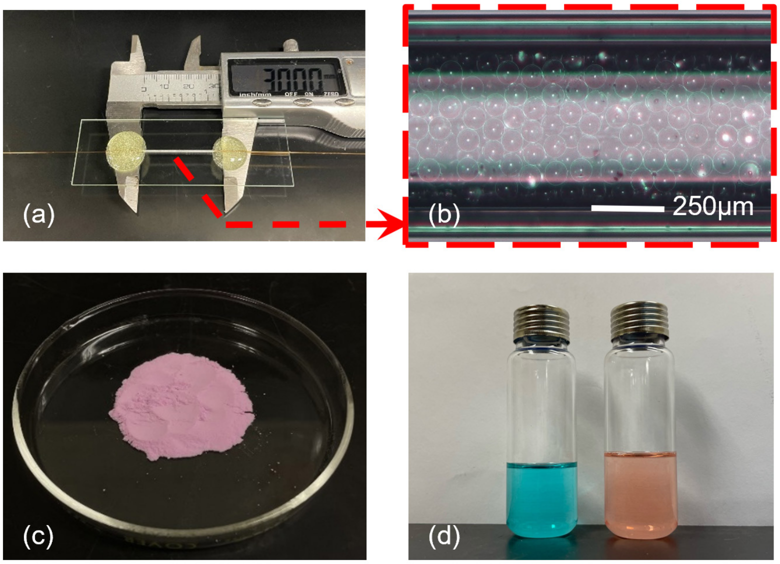

Fig. 1—(a) Picture of glass beads packed micromodel. (b) Microscope view of glass beads. (c) Fluorescent nanogel powder. (d) Fluorescent aqueous phase (blue) and fluorescent nanogel dispersion (orange).

To directly observe the inside of the 3D micromodel, the RI of the entire model should be the same, which means that the direction of refracted light can remain the same. An immersion aqueous liquid (ρ = 1920 kg/m^3; μ = 7.68 cp) was used as an aqueous phase to keep the RI the same with the quartz capillary tubes and glass beads (RI = 1.47). Then, Alexa Fluor 647 carboxylic acid was added to the immersion liquid to dye the aqueous phase and it showed a blue color. The nanogel dispersion (weight concentration of 0.05%, 0.1%, 0.15%, 0.2%, 0.25%, and 0.3%) was prepared by adding fluorescent nanogel in the immersion water and they showed red color. To make sure that nanogel dispersion was homogeneous and particles were in an almost fully swollen state, the prepared dispersion was stirred for 1 hour and then stored at 65°C for 24 hours before any characterization and experiments, as shown in **Figs. 1c and 1d**. After it had cooled to room temperature, the particle size of the nanogel dispersion was measured. The conditions under which particle size measurements were conducted were identical to those used during the injection of the nanogels into the micromodels. There is no particle collapsing because the nanogel synthesized by polyacrylamide and the crosslinker N,N′-methylenebisacrylamide are stable under 80°C and the shear rates applied during the experiments were very low.

Experimental Setup and Procedure. The visualization of fluorescent nanogel transport was achieved by a Nikon A1R-HD confocal microscope (Eclipse Ti2). We connected the micromodels to a syringe pump (Harvard Apparatus PHD ULTRATM) and a pressure transducer (Harvard Apparatus APT300 Transducer) through the flexible fused silica capillary tubes. Then, the micromodels were mounted upside down on the confocal microscope stage as shown in **Fig. 2a** for the schematic of the experimental setup. A dynamic scanning mode with a 10X objective lens was used to scan the middle section (20 mm of length, 0.5 mm of width, and 0.2 mm of depth) of the model to avoid the tubing influences at the inlet and the outlet where the beads were not being packed compactly. Using Galvano scanning, the scanning parameters that control image quality, averaging and dwell time are 1 and 1.1, respectively. The microscope stage was set to move automatically from the left outlet to the right inlet with 17 steps (20 mm) along the *x*-direction, 1 step (0.5 mm) along the *y*-direction, and 3 steps (0.129 mm) in depth along the *z*-direction constructed from 3 optical slices spaced by 43 µm. The scanning

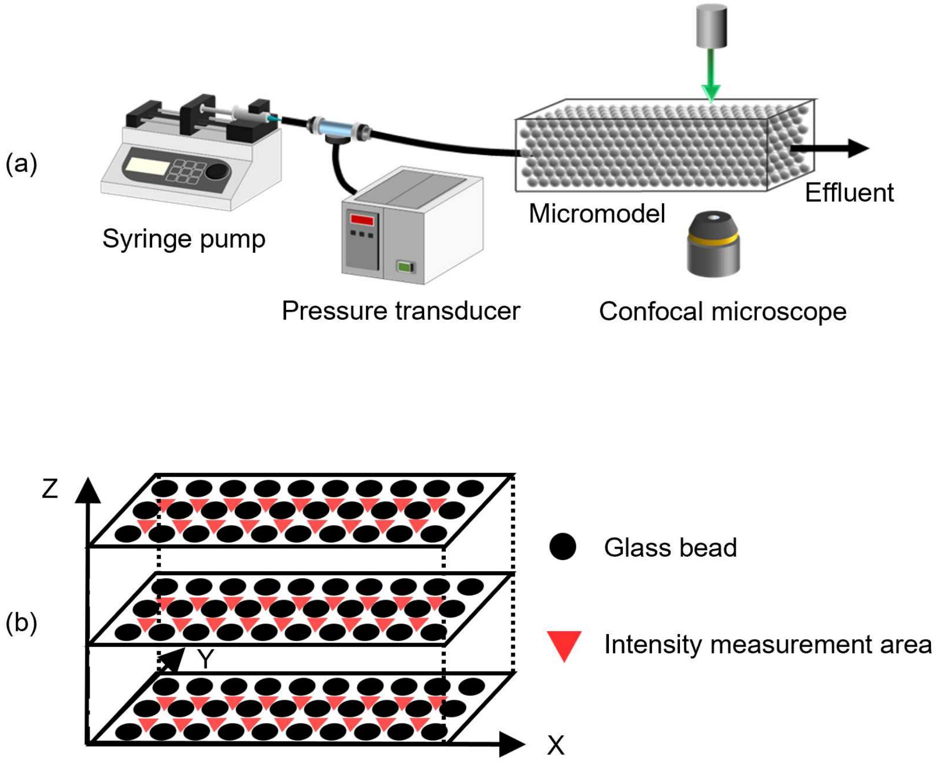

Fig. 2—(a) Schematic diagram of experimental setup. (b) Schematic diagram of intensity measurement.

area, with a length of 20 mm, is at the center of the 30-mm quartz capillary. All fields were then stitched together (5% overlap) to obtain a complete 3D image of the model.

Next, the blue-dyed immersion aqueous liquid was injected into the micromodels and permeability was measured at different flow rates (0.1 mL/h, 0.2 mL/h, 0.3 mL/h, and 0.4 mL/h). After the liquid saturation, a scanning at wavelength of 637 nm was achieved to obtain the pore structure and porosity of the micromodels. Finally, different fluorescent nanogel dispersions (weight concentration of 0.1%, 0.2%, and 0.3%) were injected into the micromodels at a flow rate of 0.01 mL/h for 6 hours [around 20 pore volume (PV) of injection]. Post-waterflooding was conducted using a flow rate of 0.01 mL/h for 10 hours for desorption. The post-waterflooding uses the same blue-dyed immersion aqueous liquid.

Concentration Determination Method. The key problem is how to determine the amount of nanogels that are not attached on the grain of porous media and can flow in pore space freely (suspended particles), which is related to the amount of nanogel that can be delivered to the target zones. However, it is hard and time-consuming to detect the tiny particles individually and count the total of particles in porous media. Thus, we focus on the concentration determination in the micromodel using the fluorescence intensity that is a reflection of a large number of particles as a whole. Because every single particle emits fluorescent light at a certain intensity when it is excited by laser (561-nm wavelength was used for the particles), there should be a relationship between particle number (concentration) and the intensity.

Therefore, we prepared six micromodels that have almost the same glass beads packing and fluorescent nanogel dispersions with different concentrations (0.05 wt%, 0.1 wt%, 0.15 wt%, 0.2 wt%, 0.25 wt%, and 0.3 wt%). Then, the six micromodels were saturated with these nanogel dispersions, respectively. After that, a Nikon A1R-HD confocal microscope (Eclipse Ti2) was used to measure the fluorescence intensity of micromodels with different concentrations. For each concentration, there were 225 measurements conducted in the pore space totally, in which five layers along the *z*-direction were measured. The depth between each layer was 43 µm and each layer included 45 measurements **(Fig. 2b)**. Then, the average intensity of each layer and model was calculated to obtain accurate values. Concentration calibration curves were built, showing the relationship between nanogel concentration and fluorescence intensity.

Results and Discussion

Nanogel Size. The size distribution of the synthesized nanogels was measured by a Malvern ZS90 Zetasizer at a scattering angle of 90° with an incident beam of a wavelength at 633 nm at 25°C. The measured sample was prepared by dispersing fluorescent nanogel in the immersion aqueous liquid with a concentration of 0.3 wt%. The size distribution of the fully swollen nanogel at 25°C is shown in **Fig. 3**, where the size range is from 33 nm to 255 nm and the number average size is 137 nm.

Concentration Calibration Curves. As we mentioned before, nanogel concentration was detected by the measurement of fluorescence intensity in micromodels. We measured the intensity profiles of six micromodels with the known concentration, and the results are shown in **Fig. 4**.

According to **Fig. 4**, it is obvious that fluorescence intensity increases linearly with fluorescent nanogel concentrations. Besides, the deeper position shows weaker fluorescence intensity because the light needs to pass through more porous media and liquid. Based on these findings, we are able to monitor the dynamic concentration distribution of micromodels in real time.

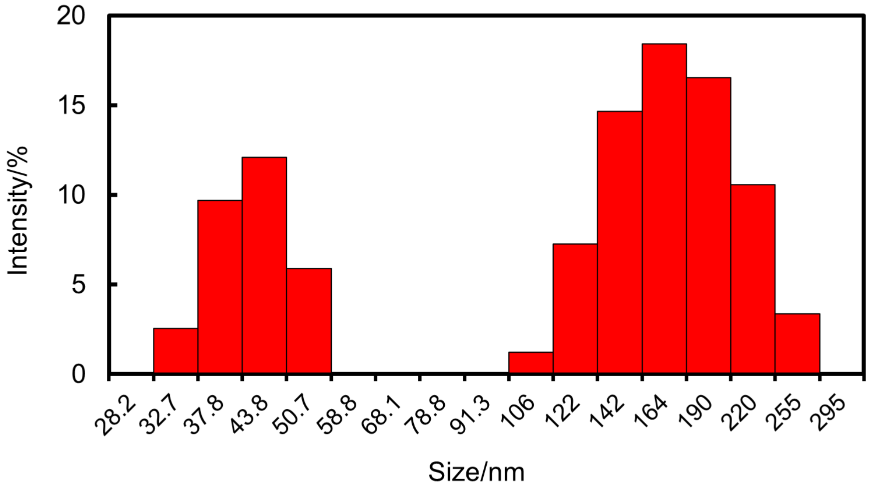

Fig. 3—Size distribution of fluorescent nanogel.

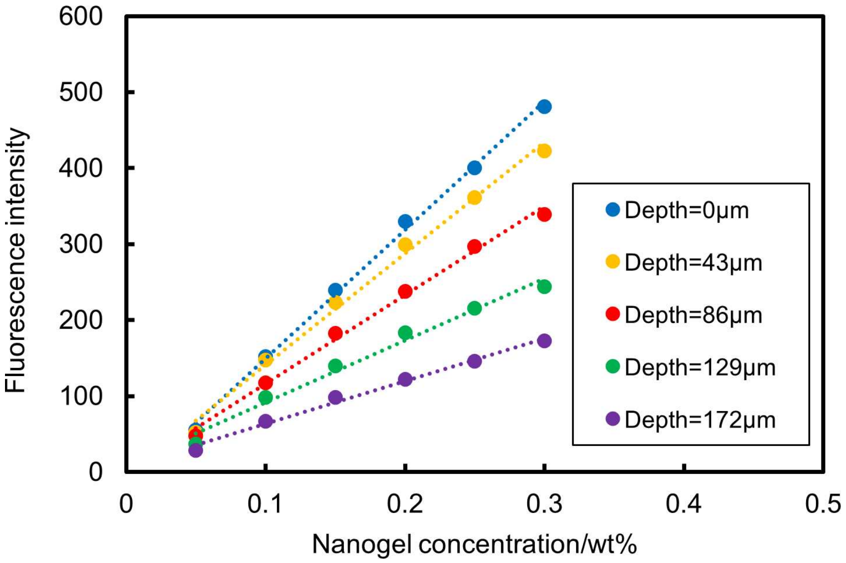

Fig. 4—Concentration calibration curve.

Concentration Distribution in Micromodel. After obtaining the linear correlation between nanogel concentration and fluorescence intensity, the injection processes of nanogel dispersions (weight concentration of 0.1%, 0.2%, and 0.3%) were recorded by the confocal microscope. **Fig. 5a** shows one of the injection processes, in which the nanogel concentration was 0.3% and the flow rate was 0.01 mL/h. **Fig. 5b** shows a local sliced 3D view of the adsorption of nanogel after post-waterflooding.

In **Fig. 5a**, the red color is nanogel dispersion and the blue color is aqueous liquid. The figure shows that there was not a clear interface or boundary between nanogel dispersion and aqueous liquid during the transport, which indicates the diffusion effect. In addition, the transition zone (the purple area where nanogel concentration ranged from 0% to maximum value) was very long in the micromodel, showing that it took nanogel some time to reach its injected concentration.

Next, we measured the intensity distribution along the micromodel and converted the intensity value to the concentration value. After comparing the intensity along vertical, lateral, and longitudinal directions, we found that the differences in intensity at vertical and lateral directions can be neglected as the ratio of length to width/height is 60. **Fig. 6** shows the longitudinal concentration distribution of 0.3% at different times during the injection process, in which the nanogel flowed from 0 cm to 2 cm. Along the flow direction, 114 measurements were conducted in the length of 2 cm.

According to **Fig. 6**, nanogel concentration decreased from 0 cm to 2 cm gradually and the whole micromodel reached 0.3% finally. We also find that the concentration distribution is not linear at the early stage of injection, but it is very close to linear later. Once linear distribution can be applied in short cores, the dynamic adsorption kinetics can be obtained in real rock porous media based on mass conservation law. Besides, **Figs. 5a and 6** strongly indicate that polymer nanogel with an average size of 137 nm transport could follow the convection-diffusion equation because the concentration distribution exhibits a very smooth transition and the concentration gradient gradually decreases over distance.

The main retention of nanogel should be adsorption because the injection pressure curves were flat and stable during the transport process as shown in **Fig. 7a**. If there were any severe plugging in the micromodel, the injection pressure would fluctuate and keep increasing until the end (Liu et al. 2022). And the resistance factor and residual resistance factor of the experiment are only 1.44 and 1.33,

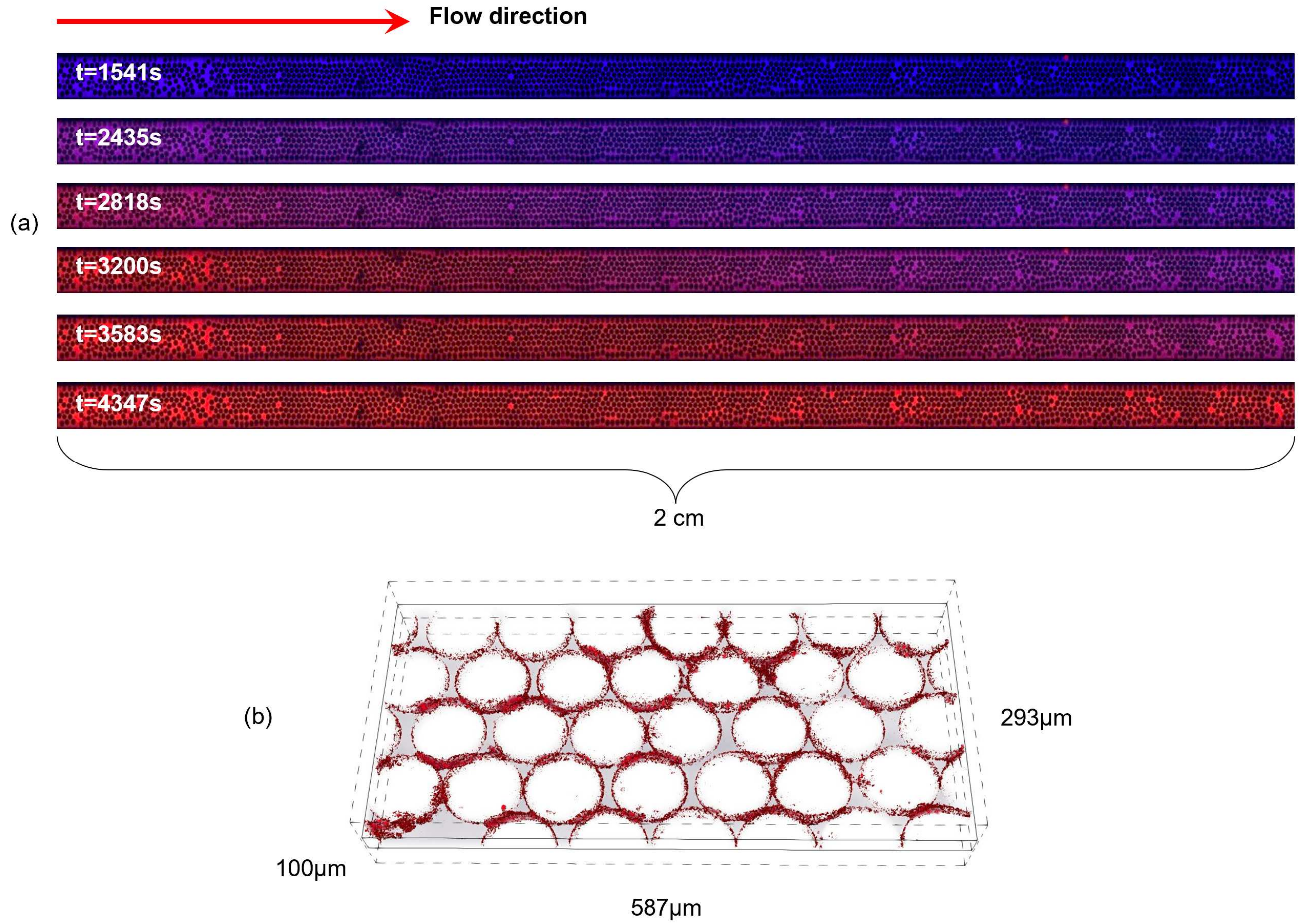

Fig. 5—(a) Global view of fluorescent nanogel (red) transport process (0.3 wt%). (b) Nanogel adsorption (red) after post-waterflooding.

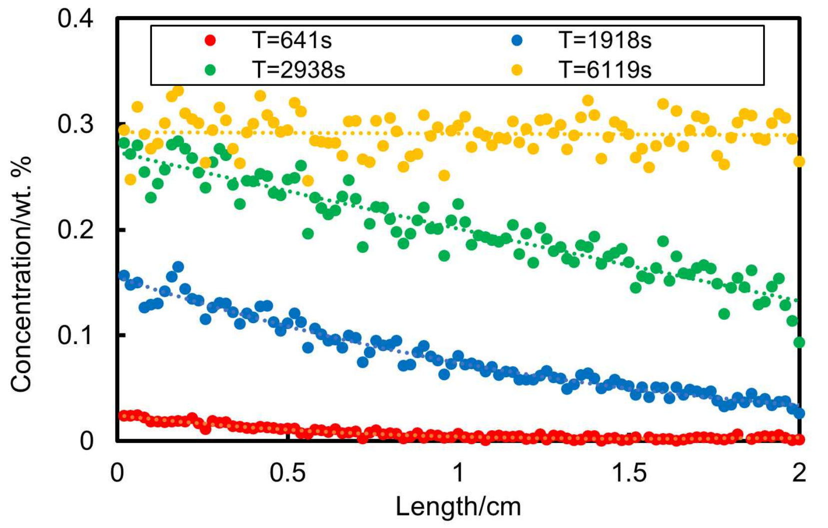

Fig. 6—Nanogel concentration distribution along the micromodel (0.3 wt%).

respectively, showing no severe plugging (see **Fig. S-3** in the Supplementary Material). Moreover, the average throat size of porous media was 5300 nm (the calculation is shown in **Fig. S-2**), which is 39 times larger than the average particle size of 137 nm. In addition, we did not find any obvious fluorescent aggregation and blocking near the pore throat as shown in **Fig. 7b**. The images of physical plugging

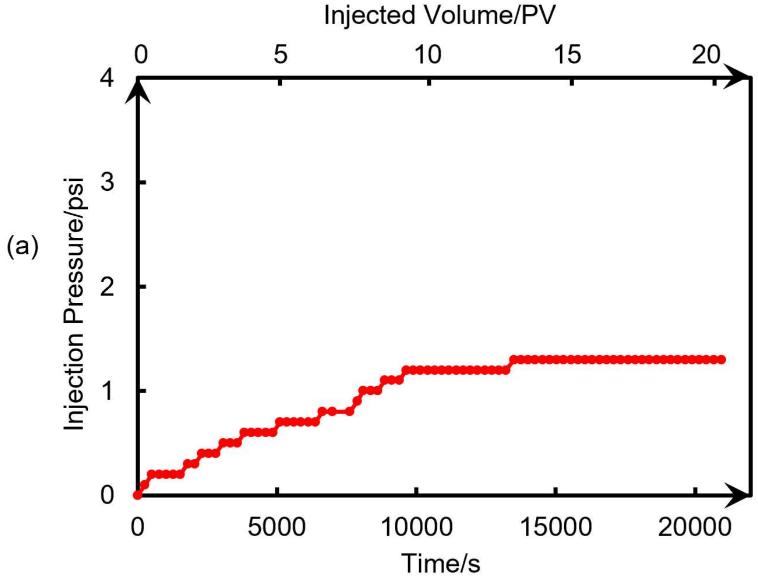

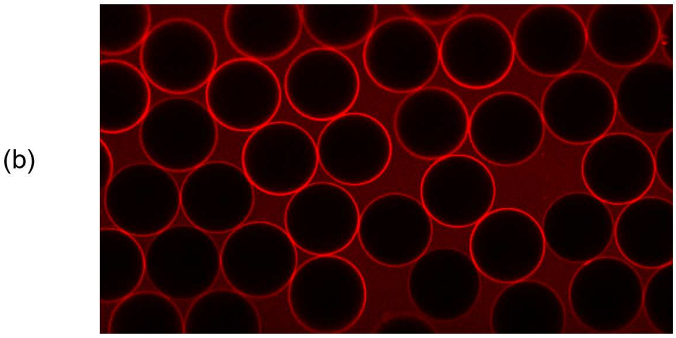

Fig. 7—(a) Nanogel injection pressure (0.3 wt%). (b) Local view of micromodel during nanogel injection (0.3 wt%).

caused by large microgel in our micromodels are very different from adsorption images, which can be compared in **Figs. S-8 through S-10**. Thus, it is reasonable to believe that adsorption is the main retention behavior.

The nanogel adsorption layer (red circle) can be observed in **Fig. 7b**, which is mainly dominated by electrostatic attraction/repulsion, hydrophilic interactions, and Van der Waals forces. The fluorescent nanogels synthesized by acrylamide are negatively charged, having repulsion with negatively charged glass beads, while the hydrophilic interactions and Van der Waals forces provide attraction for nanogels and glass beads.

Dynamic Adsorption Calculation. The dynamic adsorption was calculated by mass conservation law (Eq. 1). First, a cubic volume was selected to conduct the calculation as shown in **Fig. 8**.

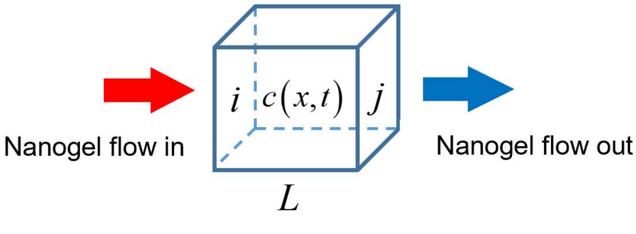

Fig. 8—Schematic diagram of dynamic adsorption calculation.

$$\Gamma(t) = \int_0^t q \times c_i(t)\,dt - \int_0^t q \times c_j(t)\,dt - \int_0^L \rho \times \phi \times A \times c(x,t)\,dx, \tag{1}$$

where $\Gamma(t)$ is the adsorption amount at time t with unit of grams; q is the flow rate; $c_i(t)$ and $c_j(t)$ are the concentrations of boundaries i and j at time t, respectively; ρ is the density of fluid; A is the cross-sectional area of micromodels; ϕ is the porosity of micromodels; and $c(x,t)$ is the concentration distribution between boundaries i and j at time t. In the equation, the first integral represents nanogels that flow into the selected volume, the second integral represents nanogels that flow out of the selected volume, and the third integral represents nanogels in pore space.

We first calculated the dynamic adsorption in the micromodel when the nanogel concentration was 0.3%. There were six continuous sections selected, including 0.4–0.6 cm, 0.6–0.8 cm, 0.8–1 cm, 1–1.2 cm, 1.2–1.4 cm, and 1.4–1.6 cm of the micromodel in length. So, the boundaries of the six selected cubic volumes (i and j) are 0.4 cm, 0.6 cm, 0.8 cm, 1 cm, 1.2 cm, 1.4 cm, and 1.6 cm from the inlet, respectively. Their concentration history $c_i\left(t\right)$ and $c_j\left(t\right)$, function of time, was measured as shown in **Fig. 9**; $c\left(x,t\right)$, the concentration distribution at different times, was already shown in **Fig. 6**.

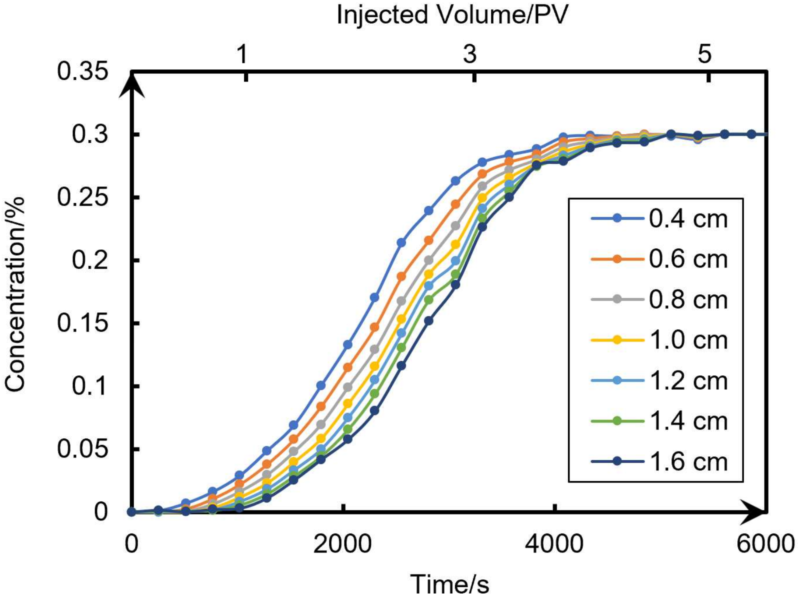

Fig. 9—Concentration history of boundaries.

In the calculation, adsorption density was defined as the adsorption mass divided by the adsorbent surface area (g/cm^2); the adsorbent surface area in the selected volume was calculated to be 0.16 cm^2 in the Supplementary Material. Because q, L, ρ, and ϕ are 0.01 mL/h, 0.2 cm, 1920 kg/m^3, and 40%, respectively, the dynamic adsorption density was calculated as shown in **Fig. 10**.

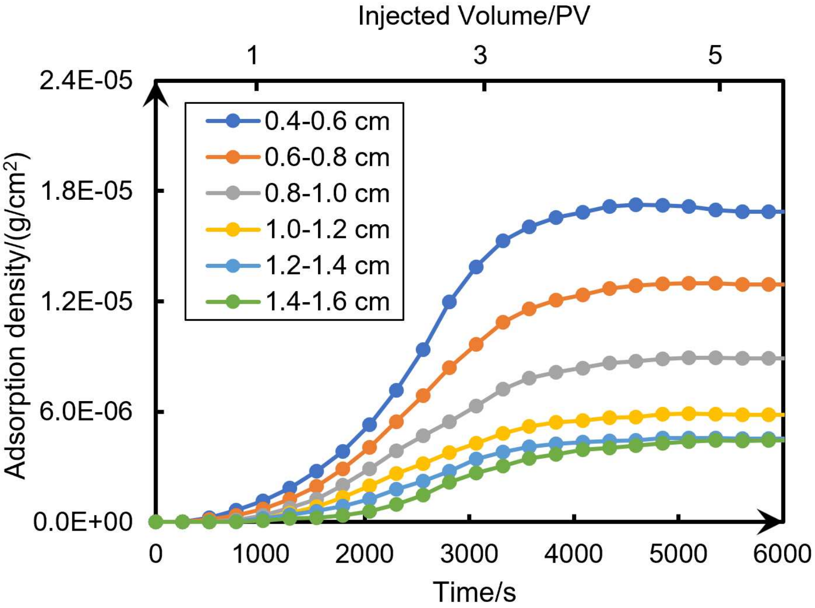

Fig. 10—Dynamic adsorption kinetics of 0.3 wt% nanogel.

Fig. 10 shows a modest initial increase rate at the very beginning, followed by a rapid growth from 1,790 seconds to 2,810 seconds. Finally, the growth rate decreased, and the equilibrium range of 3.86–16.69 µg/cm^2 was reached when the time was around 5,600 seconds. The kinetics curves are S-shaped. In addition to the time-dependent growth rate, the adsorption density is also a function of location, which is called adsorption distribution. According to **Fig. 10**, the adsorption density decreases with the increase in transport distance.

The uneven distribution was also found and investigated by many researchers in environmental science. Shapiro et al. developed a semimicroscopic stochastic theory and conducted numerical simulations for the retention profile of polydisperse particles. They showed that the temporal dispersion in the advection-dispersion reaction in deep bed filtration is the most likely reason for forming the uneven distribution (Shapiro and Bedrikovetsky 2010). However, other researchers attributed the uneven distribution to the polydispersity of particle size. Kuzmina et al. modified the deep bed filtration model for monodisperse suspension by introducing two types of particles in different sizes. They assumed that these two particles transport at different velocities and obtained the decreasing retention by the exact and asymptotic solutions (Kuzmina et al. 2017). Besides, Ma et al. built a time-distance-dependent deposition model and combined it with the advection-diffusion equation. From their simulation and experimental results, similar retention profiles were obtained and they found that the portion of large particles decreased after transport in porous media (Ma et al. 2018). Other works also show that the uneven retention profiles occurred because larger particles are more easily trapped in porous media (Ahfir et al. 2017).

To explore the reasons of uneven adsorption distribution, we measured the particle-size distribution (PSD) from the effluent during the nanogel injection process. At the beginning, when 0.025 mL (around the first 10 times of PV of the micromodel) of liquid had flowed through the micromodel, we collected it from the effluent. Then another 0.025 mL (around the second 10 times of PV of the micromodel) was collected. In total, around 20 times of pore volume (20 PV) were collected and diluted to conduct size distribution measurements. The results are shown in **Fig. 11**.

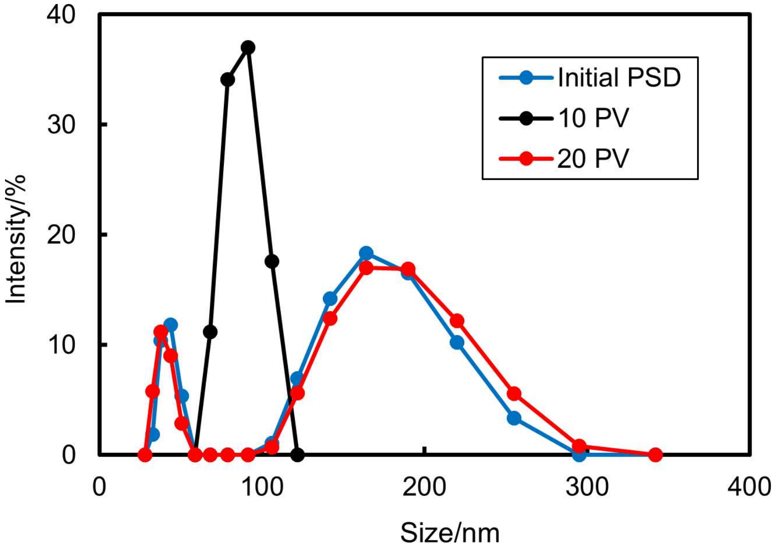

Fig. 11—PSD in the effluent of 0.3 wt%.

In **Fig. 11**, the initial PSD (blue) curves changed to a black distribution after 10 PV of injection (the peak at 100 nm appeared because the right peak of the initial PSD moved left). Because the Zetasizer cannot distinguish two peaks that are close to each other, then only a single black peak is shown in the graph. Finally, the PSD recovered to its original distribution (red) after 20 PV of injection. In terms of average particle size, the first 10 PV of nanogel (black curve) has an average particle size of 86.9 nm that is smaller than the initial average size of 137 nm (blue curve), which shows that small particles have lower adsorption than large particles. The different adsorption abilities due to particle size can be explained by the Derjaguin-Landau-Verwey-Overbeek (DLVO) theory, in which larger particles have stronger interaction energy (Zhang et al. 2015). The results indicate that large nanogel first took up the adsorption sites near the inlet then the small nanogel took up the remaining adsorption sites, causing the uneven adsorption profile. Then, the following injected nanogel would build multilayer adsorption, in which the following nanogel deposited on the first adsorption layer. It has been found that the large nanogel near the inlet might provide extra retention sites for the small nanogel, intensifying the uneven distribution (Ma et al. 2018). The injected nanogel could not keep its initial PSD until the adsorption processes were completed and the 20 PV (red curve) shows a restored particle size. Besides, the corresponding injection time of 10 PV is 2.5 hours, which is close to the time that the whole micromodel can reach adsorption equilibrium. In other words, the first 10 PV of nanogel experienced PSD change due to adsorption, while the 10–20 PV of nanogel did not. The time of 2.5 hours in **Fig. 11** validates the equilibrium time of adsorption kinetics in **Fig. 10**.

In addition to dynamic adsorption kinetics, the method can also be used to show desorption kinetics during the post-waterflooding process. Similarly, the desorption process was also investigated using the mass conservation equation:

$$\Gamma\left(t\right)' = \int_0^L \rho \times \phi \times A \times c_o dx + \Gamma_o + \int_0^t q \times c_i\left(t\right) dt - \int_0^t q \times c_j\left(t\right) dt - \int_0^L \rho \times \phi \times A \times c\left(x,t\right) dx, \qquad (2)$$

where $\Gamma\left(t\right)'$ is the remaining nanogel during desorption, c_o is the nanogel concentration before post-waterflooding (the nanogel concentration injected), Γ_o is the equilibrium nanogel adsorption amount before desorption. Because c_o, q, L, ρ, and ϕ were 0.3%, 0.01 mL/h, 0.2 cm, 1.921 g/mL, and 40%, respectively, the dynamic desorption was calculated as shown in **Fig. 12**.

According to **Fig. 12**, there is a modest decrease at the beginning, followed by a rapid decrease from 1,530 seconds to 2,551 seconds and a slow reduction from 2,551 seconds to 4,846 seconds. Finally, the equilibrium range of 2.13–9.69 μg/cm^2 was reached when the time was around 5,000 seconds. Compared with **Fig. 10**, around 45% of adsorption was removed in all the measured sections during post-waterflooding. The desorption distribution shows a similar variation to **Fig. 10** because the reversible adsorption is around 45% of the adsorbed nanogel in these micromodels.

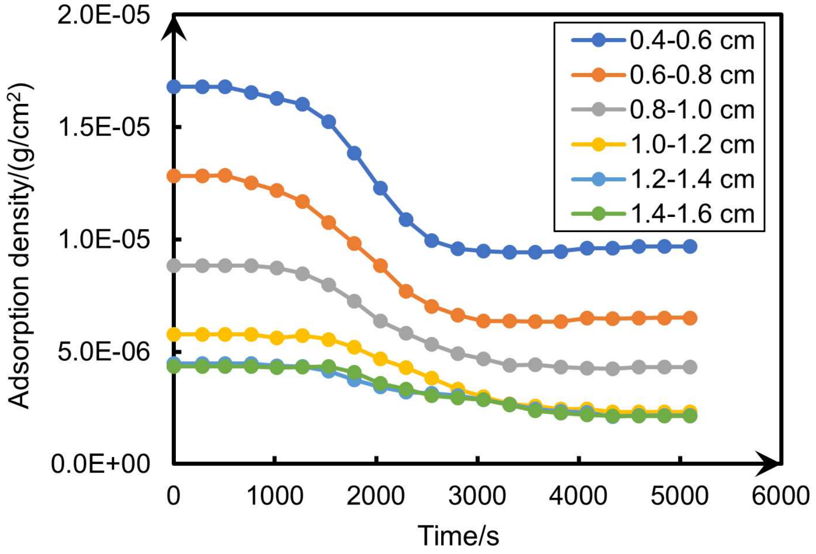

Fig. 12—Dynamic desorption kinetics of 0.3 wt% nanogel.

Factors Influencing Adsorption Distribution. To further investigate the factors influencing dynamic adsorption, we used different nanogel concentrations (0.1 wt% and 0.2 wt%) and different flow rates (0.02 mL/h and 0.03 mL/h, nanogel concentration is 0.2 wt%) and calculated the adsorption results as shown in **Figs. 13a through 13d**. The pressure of nanogel injection and post-waterflooding is shown in the Supplementary Material (**Figs. S-4 through S-7**).

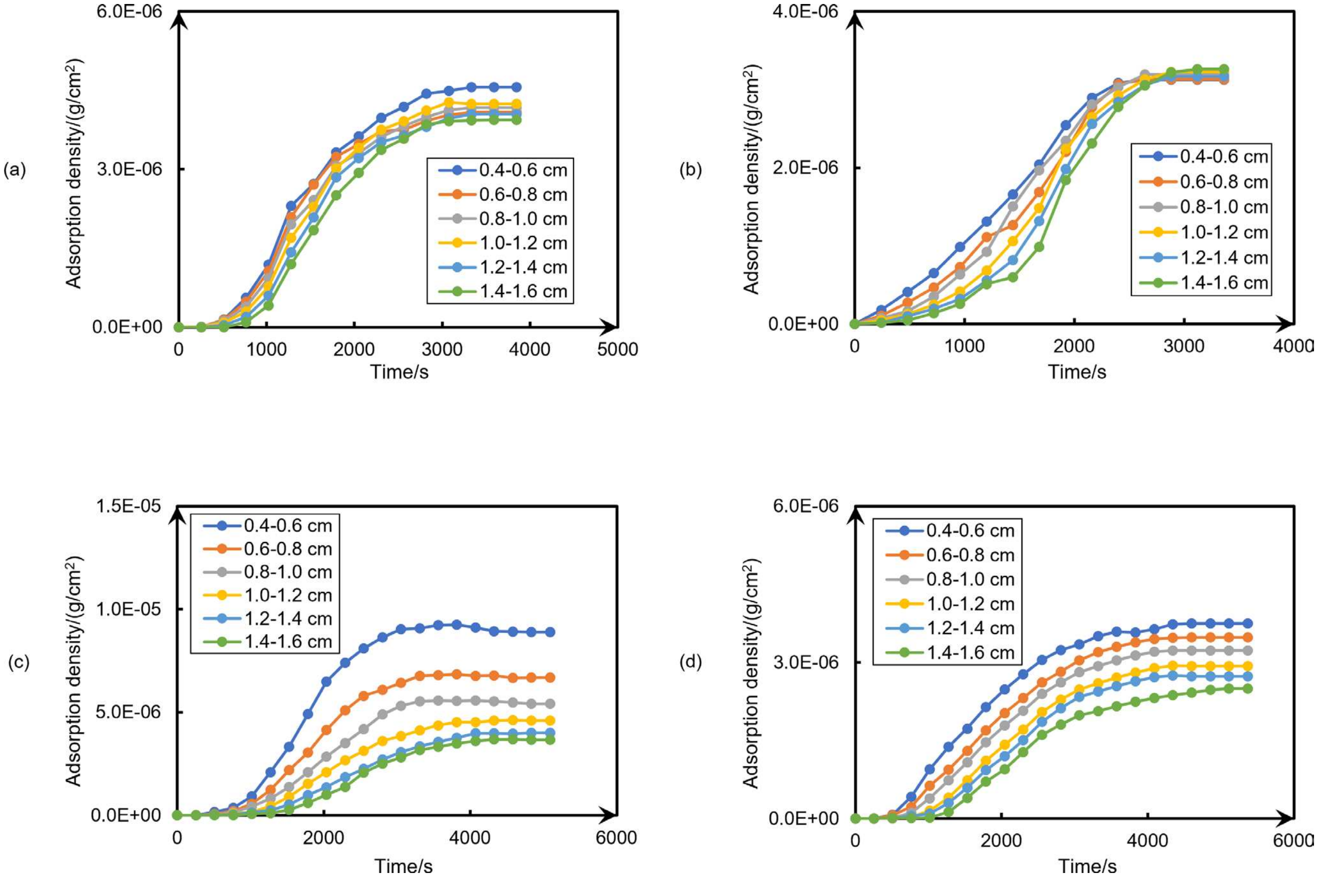

Fig. 13—(a) Dynamic adsorption kinetics of 0.1 wt%. (b) Dynamic adsorption kinetics of 0.2 wt%. (c) Dynamic adsorption kinetics of 0.02 mL/h with 0.2 wt%. (d) Dynamic adsorption kinetics of 0.03 mL/h with 0.2 wt%.

According to **Figs. 13a and 13b**, the higher concentration leads to more dynamic adsorption in the micromodels, which is consistent with many adsorption models, including linear (Johnson and Elimelech 1995) and nonlinear isothermal adsorption models (Zhang et al. 2018; Bai et al. 2019). Compared with **Figs. 10, 13a, and 13d**, it is found that a higher flow rate results in less dynamic adsorption. These findings could be explained by the theory of removal efficiency in physicochemical particle filtration in porous media (Ryan and Elimelech 1996; Tufenkji and Elimelech 2004), in which adsorption density (particle removal efficiency of glass beads) is inversely proportional to flow velocity and particle concentration.

In addition, to compare the adsorption profiles at different conditions, we introduced a coefficient of variation from statistics that is used to describe the uniformity of adsorption distribution. It is defined as the ratio of the standard deviation to the mean:

$$C_v = \frac{\sigma}{\mu}, \tag{3}$$

where C_v is the coefficient of variation and σ and μ are the standard deviation and the mean value of the adsorption density values in six continuous intervals, respectively. According to its definition, severe uneven distribution would have a higher coefficient of variation. Then, the adsorption profiles can be compared in **Fig. 14**.

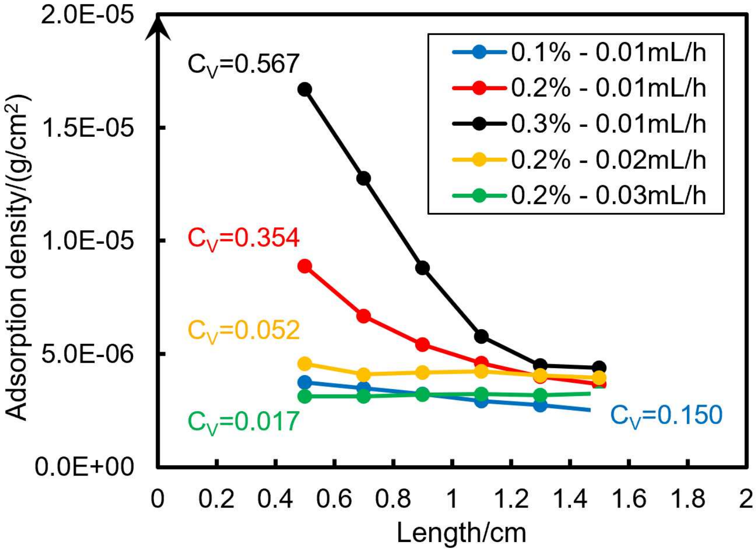

Fig. 14—Comparison of adsorption profiles.

Fig. 14 shows that lower concentration and higher flow rate can attenuate the uneven distribution of adsorption. The possible reason is that lower concentration means less large nanogel, so there were fewer extra retention sites for the small nanogel, failing to intensify the uneven distribution. The low-velocity effect can be explained by two adsorption regions, including diffusion region and adsorption region as shown in **Fig. 15**.

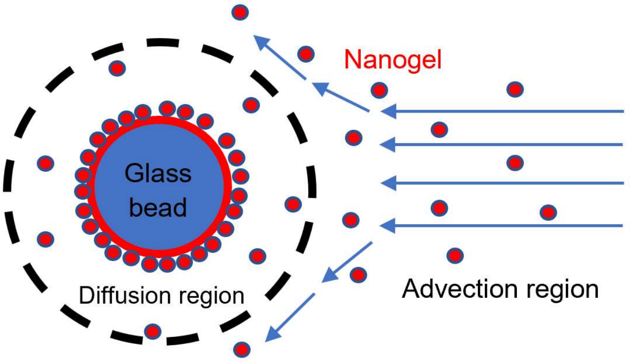

Fig. 15—Possible adsorption process.

Ryan et al. described a diffusion boundary layer based on the DLVO theory. The layer is defined as the near-surface region in which colloid adsorption is dominated by diffusion. Beyond the diffusion boundary layer, colloid transport is controlled by the advection of the bulk fluid. (In **Fig. 7b**, the adsorption layer on glass beads is very similar to the model in **Fig. 15**.) The rate of colloid transport across the boundary layer is controlled by diffusion coefficient, concentration gradient, and the thickness of the boundary layer, which is controlled mainly by fluid velocity (Ryan and Elimelech 1996). When we increased the flow rate, the diffusion boundary layer thickness decreased, and advection dominated the transport and adsorption of nanogel. Although the different adsorption abilities from different nanogel sizes remained, their influence was significantly weakened in the whole region. Therefore, the adsorption distribution became homogeneous.

Conclusions

Overall, we presented a novel method to study nanogel particle adsorption and desorption in porous media using 3D glass micromodels and confocal microscopy. Based on the experimental results and analysis above, the following conclusions can be reached.

1. The real-time transport of polymer nanogel was visualized in porous media and nanogel with an average size of 137 nm can flow through the micromodels that have a throat size of 5.3 μm without obvious physical plugging.
2. Fluorescence intensity increases linearly with fluorescent nanogel concentration, which can be used to determine nanogel concentration profiles in transparent micromodels. Nanogel concentration distribution is not linear at a long distance, but it is very close to linear at a short distance, which provides a method to calculate dynamic adsorption kinetics in real rock material.
3. Nanogel adsorption kinetics shows S-shaped curves, and the equilibrium adsorption density varies from 2.49 $\mu g/cm^2$ to 16.69 $\mu g/cm^2$ for borosilicate glass in immersion liquid. The desorption removed nearly 45% of nanogel of adsorption.
4. Dynamic adsorption is a function of both time and location, and it increases with higher concentration and lower flow rate. The size distribution change from the effluent reveals that different sizes of nanogels have different adsorption abilities. Moreover, the uneven distribution can be attenuated by decreasing nanogel concentration or increasing flow rate.
5. The results strongly indicate that polymer nanogel transport in porous media could be modeled by convection-diffusion equation combined with adsorption/desorption kinetics.

In terms of the method, there are some works that can be performed in the future to improve it. First, the particle types can be extended to other colloids, such as silica-based gel particles. Second, it is more realistic to have micromodels made of rock materials that can provide adsorption and desorption at reservoir conditions (high pressure and temperature). Third, the data acquisition and processing should be accomplished automatically by more advanced softwares so that the particle transport and adsorption quantification can be performed much faster and easier.

Nomenclature

A = cross-sectional area of micromodels, cm^2
$c_i(t)$ = nanogel concentration of boundary i at time t, wt%
$c_j(t)$ = nanogel concentration of boundary j at time t, wt%
c_v = coefficient of variation, dimensionless
$c(x,t)$ = nanogel concentration of location x at time t, wt%
C_o = flow rate, mL/h
L = length of micromodels, cm
q = flow rate, mL/h
x = distance from inlet, cm
Γ = nanogel adsorption amount during injection, g
Γ_o = equilibrium nanogel adsorption amount before desorption, g
Γ' = nanogel adsorption amount during desorption, g
ϕ = micromodel porosity, %
ρ = density of the fluid, g/mL

Acknowledgments

The authors would like to acknowledge the National Science Foundation for funding through grants DMS-1722647 and DMS-2152609, as well as the Qatar National Research Fund (a member of Qatar Foundation) for funding through Grant # NPRP13S-1231-190009.

References

Ahfir, N.-D., Hammadi, A., Alem, A. et al. 2017. Porous Media Grain Size Distribution and Hydrodynamic Forces Effects on Transport and Deposition of Suspended Particles. *J Environ Sci (China)* **53**: 161–172. https://doi.org/10.1016/j.jes.2016.01.032.

Almohsin, A., Bai, B., and Imqam, A. 2014. Transport of Nanogel through Porous Media and Its Resistance to Water Flow. Paper presented at the SPE Improved Oil Recovery Symposium, Tulsa, Oklahoma, USA, 12−16 April. https://doi.org/10.2118/169078-MS.

Bai, B., Rao, D., Chang, T. et al. 2019. A Nonlinear Attachment-Detachment Model with Adsorption Hysteresis for Suspension-Colloidal Transport in Porous Media. *J Hydrol* **578**: 124080. https://doi.org/10.1016/j.jhydrol.2019.124080.

Cao, D., Han, M., Wang, J. et al. 2020. Optimization of Microsphere Injection by Balancing the Blocking and Migration Capacities in a Heterogeneous Carbonate Matrix. Paper presented at the Abu Dhabi International Petroleum Exhibition & Conference, Abu Dhabi, UAE, 9−12 November. https://doi.org/10.2118/203131-MS.

Chan, M. and Almutairi, A. 2016. Nanogels as Imaging Agents for Modalities Spanning the Electromagnetic Spectrum. *Mater Horiz* **3** (1): 21–40. https://doi.org/10.1039/c5mh00161g.

Chauveteau, G., Tabary, R., Blin, N. et al. 2004. Disproportionate Permeability Reduction by Soft Preformed Microgels. Paper presented at the SPE/DOE Symposium on Improved Oil Recovery, Tulsa, Oklahoma, USA, 17−21 April. https://doi.org/10.2118/89390-MS.

Chauveteau, G., Tabary, R., Bon, C. le. et al. 2003. In-Depth Permeability Control by Adsorption of Soft Size-Controlled Microgels. Paper presented at the SPE European Formation Damage Conference, The Hague, Netherlands, 13−14 May. https://doi.org/10.2118/82228-MS.

Chen, X., Li, Y., Liu, Z. et al. 2020a. Core- and Pore-Scale Investigation on the Migration and Plugging of Polymer Microspheres in a Heterogeneous Porous Media. *J Pet Sci Eng* **195** (June): 107636. https://doi.org/10.1016/j.petrol.2020.107636.

Chen, X., Li, Y., Liu, Z. et al. 2020b. Mechanism Investigation and Optimization of Conformance Control by Polymer Microsphere in Heterogeneous Offshore Oil Fields. Paper presented at the Offshore Technology Conference Asia, Kuala Lumpur, Malaysia, 2−6 November. https://doi.org/10.4043/30200-MS.

Chen, Y., Tang, Z., Wang, S. et al. 2022. Fluorescent Polyacrylamide Nanospheres for Concentration Detection and Fluorescent Visual Oil Displacement Experiments. *J Appl Polym Sci* **139** (14). https://doi.org/10.1002/app.51898.

Cozic, C., Rousseau, D., and Tabary, R. 2008. Broadening the Application Range of Water Shutoff / Conformance Control Microgels: An Investigation of Their Chemical Robustness. Paper presented at the SPE Annual Technical Conference and Exhibition, Denver, Colorado, USA, 21−24 September. https://doi.org/10.2118/115974-MS.

Dai, C., Liu, Y., Zou, C. et al. 2017. Investigation on Matching Relationship between Dispersed Particle Gel (DPG) and Reservoir Pore-Throats for in-Depth Profile Control. *Fuel (Lond)* **207**: 109–120. https://doi.org/10.1016/j.fuel.2017.06.076.

Ding, H. 2020. *Factors Impacting the Transport and Enhanced Oil Recovery Potential of Polymeric Nanogel in Sandstone*. Rolla, Missouri, USA: Missouri University of Science and Technology.

Ding, H., Geng, J., Lu, Y. et al. 2020. Impacts of Crosslinker Concentration on Nanogel Properties and Enhanced Oil Recovery Capability. *Fuel (Lond)* **267**: 117098. https://doi.org/10.1016/j.fuel.2020.117098.

El-Diasty, A. I. and Aly, A. M. 2015. Understanding the Mechanism of Nanoparticles Applications in Enhanced Oil Recovery. Paper presented at the SPE North Africa Technical Conference and Exhibition, Cairo, Egypt, 14−16 September. https://doi.org/10.2118/175806-MS.

Feng, Y., Tabary, R., Renard, M. et al. 2003. Characteristics of Microgels Designed for Water Shutoff and Profile Control. Paper presented at the International Symposium on Oilfield Chemistry, Houston, Texas, USA, 5−7 February. https://doi.org/10.2118/80203-MS.

Gaol, C. L., Wegner, J., and Ganzer, L. 2020. Real Structure Micromodels Based on Reservoir Rocks for Enhanced Oil Recovery (EOR) Applications. *Lab Chip* **20** (12): 2197–2208. https://doi.org/10.1039/d0lc00257g.

Geng, J., Ding, H., Han, P. et al. 2018. Transportation and Potential Enhanced Oil Recovery Mechanisms of Nanogels in Sandstone. *Eng Fuels* **32** (8): 8358–8365. https://doi.org/10.1021/acs.energyfuels.8b01873.

Geng, J., Shi, X., Han, P. et al. 2020. Experimental Study on Charged Nanogels for Interfacial Tension Reduction and Emulsion Stabilization at Various Salinities and Oil Types. *Eng Fuels* **34** (12): 15894–15904. https://doi.org/10.1021/acs.energyfuels.0c02591.

Han, P., Geng, J., and Bai, B. 2019. Investigation on Transport Behavior of Nanogel in Low Permeable Porous Medium. *J Pet Sci Eng* **178** (April): 999–1005. https://doi.org/10.1016/j.petrol.2019.04.020.

Han, P., Geng, J., Ding, H. et al. 2020. Experimental Study on the Synergistic Effect of Nanogel and Low Salinity Water on Enhanced Oil Recovery for Carbonate Reservoirs. *Fuel (Lond)* **265**: 116971. https://doi.org/10.1016/j.fuel.2019.116971.

He, J., Shao, M., Yue, X. et al. 2021. Fabrication and Characteristics of Self-Aggregation Nanoparticles Used for Conformance Control Treatment. *Polym Adv Techs* **32** (1): 190–201. https://doi.org/10.1002/pat.5074.

Hou, G., Yuan, X., Han, P. et al. 2020. Field Application of Nano Polymer Microspheres Profile Control: A Pilot Test in Ultra-Low Permeability Oil Reservoir. Paper presented at the SPE Asia Pacific Oil & Gas Conference and Exhibition, Virtual, 17−19 November. https://doi.org/10.2118/202412-MS.

Hua, Z., Lin, M., Dong, Z. et al. 2014. Study of Deep Profile Control and Oil Displacement Technologies with Nanoscale Polymer Microspheres. *J Colloid Interface Sci* **424**: 67–74. https://doi.org/10.1016/j.jcis.2014.03.019.

Jia, H., Ren, Q., Pu, W.-F. et al. 2014. Swelling Mechanism Investigation of Microgel with Double-Cross-Linking Structures. *Eng Fuels* **28** (11): 6735–6744. https://doi.org/10.1021/ef5012325.

Johnson, P. R. and Elimelech, M. 1995. Dynamics of Colloid Deposition in Porous Media: Blocking Based on Random Sequential Adsorption. *Langmuir* **11** (3): 801–812. https://doi.org/10.1021/la00003a023.

Kuzmina, L. I., Osipov, Y. V., and Galaguz, Y. P. 2017. A Model of Two-Velocity Particles Transport in A Porous Medium. *Int J Non Linear Mech* **93** (April): 1–6. https://doi.org/10.1016/j.ijnonlinmec.2017.04.015.

Lehoux, A. P., Faure, P., Michel, E. et al. 2017. Transport and Adsorption of Nano-Colloids in Porous Media Observed by Magnetic Resonance Imaging. *Transp Porous Med* **119** (2): 403–423. https://doi.org/10.1007/s11242-017-0890-4.

Lenchenkov, N. S. 2017. *Conformance Control in Heterogeneous Oil Reservoirs with Polymer Gels and Nano Spheres*. Doctoral Thesis, Delft University of Technology, Delft, The Netherlands. https://doi.org/10.4233/uuid:1686e932-2df7-41df-80af-643d5a34fb2f.

Li, S. 2016. *Study on Plugging and Migration of Cross-Linked Polymer Microspheres*. Beijing, China: China University of Petroleum-Beijing.

Li, J., Niu, L., and Lu, X. 2019. Migration Characteristics and Deep Profile Control Mechanism of Polymer Microspheres in Porous Media. *Energy Sci Eng* **7** (5): 2026–2045. https://doi.org/10.1002/ese3.409.

Li, S., Yu, H. H., and Fan, J. 2021a. Modeling Transport of Soft Particles in Porous Media. *Phys Rev E* **104** (2–2): 025112. https://doi.org/10.1103/PhysRevE.104.025112.

Li, S., Yu, H., Li, T.-D. et al. 2020. Understanding Transport of an Elastic, Spherical Particle through a Confining Channel. *Appl Phys Lett* **116** (10). https://doi.org/10.1063/1.5139887.

Li, Z., Zhao, T., Lv, W. et al. 2021b. Nanoscale Polyacrylamide Copolymer/Silica Hydrogel Microspheres with High Compressive Strength and Satisfactory Dispersion Stability for Efficient Profile Control and Plugging. *Ind Eng Chem Res* **60** (28): 10193–10202. https://doi.org/10.1021/acs.iecr.1c01617.

Liang, T., Hou, J., Qu, M. et al. 2019. The EOR Mechanism and Flow Behaviors of High-Viscosity Modified Starch Nanogel Particles in Porous Media. Paper presented at the SPE/IATMI Asia Pacific Oil & Gas Conference and Exhibition, Bali, Indonesia, 29−31 October. https://doi.org/10.2118/196414-MS.

Liu, J., Almakimi, A., Wei, M. et al. 2022. A Comprehensive Review of Experimental Evaluation Methods and Results of Polymer Micro/Nanogels for Enhanced Oil Recovery and Reduced Water Production. *Fuel (Lond)* **324**: 124664. https://doi.org/10.1016/j.fuel.2022.124664.

Liu, C., Liao, X., Zhang, Y. et al. 2012. Field Application of Polymer Microspheres Flooding: A Pilot Test in Offshore Heavy Oil Reservoir. Paper presented at the SPE Annual Technical Conference and Exhibition, San Antonio, Texas, USA, 8−10 October. https://doi.org/10.2118/158293-MS.

Ma, E., Ouahbi, T., Wang, H. et al. 2018. Modeling of the Transport and Deposition of Polydispersed Particles: Effects of Hydrodynamics and Spatiotemporal Evolution of the Deposition Rate. *Environ Pollut* **237**: 1011–1022. https://doi.org/10.1016/j.envpol.2017.11.017.

Qiu, Y., Wei, M., Bai, B. et al. 2017. Data Analysis and Application Guidelines for the Microgel Field Applications. *Fuel (Lond)* **210** (May): 557–568. https://doi.org/10.1016/j.fuel.2017.08.094.

Rousseau, D., Chauveteau, G., Renard, M. et al. 2005. Rheology and Transport in Porous Media of New Water Shutoff/Conformance Control Microgels. Paper presented at the SPE International Symposium on Oilfield Chemistry, The Woodlands, Texas, USA, 2−4 February. https://doi.org/10.2118/93254-MS.

Ryan, J. N. and Elimelech, M. 1996. Colloid Mobilization and Transport in Groundwater. *Colloids Surf A: Physicochem Eng Aspects* **107** (95): 1–56. https://doi.org/10.1016/0927-7757(95)03384-X.

Seright, R. S. and Liang, J. 1995. A Comparison of Different Types of Blocking Agents. Paper presented at the SPE European Formation Damage Conference, The Hague, Netherlands, 15−16 May. https://doi.org/10.2118/30120-MS.

Shapiro, A. A. and Bedrikovetsky, P. G. 2010. A Stochastic Theory for Deep Bed Filtration Accounting for Dispersion and Size Distributions. *Physica A Stat Mech Appl* **389** (13): 2473–2494. https://doi.org/10.1016/j.physa.2010.02.049.

Shi, X. and Yue, X. 2020. Migration and Plugging Mechanisms of Self-Aggregated Microspheres as a Novel Profile Control. *J Pet Sci Eng* **184**: 106458. https://doi.org/10.1016/j.petrol.2019.106458.

Sivaram, A. J., Rajitha, P., Maya, S. et al. 2015. Nanogels for Delivery, Imaging and Therapy. *Wiley Interdiscip Rev Nanomed Nanobiotechnol* **7** (4): 509–533. https://doi.org/10.1002/wnan.1328.

Sun, Z., Kang, X., Na, R. et al. 2020. Research on the Reservoir Adaptability and Oil Displacement Mechanism of a New Soft Microgel Particle Dispersion System. Paper presented at the SPE Russian Petroleum Technology Conference, Virtual, 26−29 October. https://doi.org/10.2118/201839-MS.

Sun, Z., Kang, X., Tang, X. et al. 2018. Performance Evaluation and Field Trial of Self-Adaptive Microgel Flooding Technology. Paper presented at the Abu Dhabi International Petroleum Exhibition & Conference, Abu Dhabi, UAE, 12–15 November. https://doi.org/10.2118/192651-MS.

Sun, X., Zhang, Y., Chen, G. et al. 2017. Application of Nanoparticles in Enhanced Oil Recovery: A Critical Review of Recent Progress. *Energies* **10** (3): 345. https://doi.org/10.3390/en10030345.

Tian, Y., Wang, L., Tang, Y. et al. 2012. Research and Application of Nano Polymer Microspheres Diversion Technique of Deep Fluid. Paper presented at the SPE International Oilfield Nanotechnology Conference and Exhibition, Noordwijk, The Netherlands, 12–14 June. https://doi.org/10.2118/156999-MS.

Tufenkji, N. and Elimelech, M. 2004. Correlation Equation for Predicting Single-Collector Efficiency in Physicochemical Filtration in Saturated Porous Media. *Environ Sci Technol* **38** (2): 529–536. https://doi.org/10.1021/es034049r.

Wang, S., Tang, Z., Qu, J. et al. 2021. Research on the Mechanisms of Polyacrylamide Nanospheres with Different Size Distributions in Enhanced Oil Recovery. *RSC Adv* **11** (10): 5763–5772. https://doi.org/10.1039/D0RA09348C.

Wu, D., Liu, Y., Lu, X. et al. 2022. Study on Blockage and Fluid Diversion Behaviors of Polymer Microspheres. Paper presented at the SPE EuropEC - Europe Energy Conference Featured at the 83rd EAGE Annual Conference & Exhibition, Madrid, Spain, 6–9 June. https://doi.org/10.2118/209706-MS.

Wu, T., Zhao, K., Liu, S. et al. 2023. Promising Nanocarriers Endowing Non-Systemic Pesticides with Upward Translocation Ability and Microbial Community Enrichment Effects in Soil. *Chem Eng J* **474** (August): 145570. https://doi.org/10.1016/j.cej.2023.145570.

Wu, D., Zhou, K., Hou, J. et al. 2021. Review of Experimental and Simulation Studies of Enhanced Oil Recovery Using Viscoelastic Particles. *J Dispers Sci Technol* **42** (7): 956–969. https://doi.org/10.1080/01932691.2020.1723620.

Xu, S., Gao, B., and Saiers, J. E. 2006. Straining of Colloidal Particles in Saturated Porous Media. *Water Resour Res* **42** (12): 1–10. https://doi.org/10.1029/2006WR004948.

Yao, C., Lei, G., Cathles, L. M. et al. 2014. Pore-Scale Investigation of Micron-Size Polyacrylamide Elastic Microspheres (MPEMs) Transport and Retention in Saturated Porous Media. *Environ Sci Technol* **48** (9): 5329–5335. https://doi.org/10.1021/es500077s.

Yao, C., Lei, G., Hou, J. et al. 2015. Enhanced Oil Recovery Using Micron-Size Polyacrylamide Elastic Microspheres: Underlying Mechanisms and Displacement Experiments. *Ind Eng Chem Res* **54** (43): 10925–10934. https://doi.org/10.1021/acs.iecr.5b02717.

Yao, C., Lei, G., Li, L. et al. 2012. Selectivity of Pore-Scale Elastic Microspheres as a Novel Profile Control and Oil Displacement Agent. *Eng Fuels* **26** (8): 5092–5101. https://doi.org/10.1021/ef300689c.

Yao, C., Liu, B., Li, L. et al. 2020. Transport and Retention Behaviors of Deformable Polyacrylamide Microspheres in Convergent-Divergent Microchannels. *Environ Sci Technol* **54** (17): 10876–10884. https://doi.org/10.1021/acs.est.0c02243.

Yao, C., Xu, X., Wang, D. et al. 2016. Research and Application of Micron-Size Polyacrylamide Elastic Microspheres as a Smart Sweep Improvement and Profile Modification Agent. Paper presented at the SPE Improved Oil Recovery Conference, Tulsa, Oklahoma, USA, 11–13 April. https://doi.org/10.2118/179531-MS.

Yu, Z., Li, Y., Sha, O. et al. 2016. Synthesis and Properties of Amphiprotic Polyacrylamide Microspheres as Water Shutoff and Profile Control. *J Appl Polym Sci* **133** (17). https://doi.org/10.1002/app.43366.

Yuan, C., Pu, W., Varfolomeev, M. A. et al. 2021. Deformable Microgel for Enhanced Oil Recovery in High-Temperature and Ultrahigh-Salinity Reservoirs: How to Design the Particle Size of Microgel to Achieve Its Optimal Match with Pore Throat of Porous Media. *SPE J.* **26** (4): 2053–2067. https://doi.org/10.2118/197804-PA.

Zhang, Y., Bland, G. D., Yan, J. et al. 2021a. Amphiphilic Thiol Polymer Nanogel Removes Environmentally Relevant Mercury Species from Both Produced Water and Hydrocarbons. *Environ Sci Technol* **55** (2): 1231–1241. https://doi.org/10.1021/acs.est.0c05470.

Zhang, Y., Geng, J., Liu, J. et al. 2021b. Direct Pore-Level Visualization and Verification of In Situ Oil-in-Water Pickering Emulsification during Polymeric Nanogel Flooding for EOR in a Transparent Three-Dimensional Micromodel. *Langmuir* **37** (45): 13353–13364. https://doi.org/10.1021/acs.langmuir.1c02029.

Zhang, H., Malgaresi, G. V. C., and Bedrikovetsky, P. 2018. Exact Solutions for Suspension-Colloidal Transport with Multiple Capture Mechanisms. *Int J Non Linear Mech* **105** (June): 27–42. https://doi.org/10.1016/j.ijnonlinmec.2018.07.007.

Zhang, T., Murphy, M. J., Yu, H. et al. 2015. Investigation of Nanoparticle Adsorption During Transport in Porous Media. *SPE J.* **20** (4): 667–677. https://doi.org/10.2118/166346-PA.

Zhou, Y., Luo, Z., Xu, M. et al. 2023. Preparation and Properties of Temperature-Sensitive P(NIPAM-AM) Nano–Microspheres in Enhanced Oil Recovery. *Eng Fuels* **37** (1): 204–213. https://doi.org/10.1021/acs.energyfuels.2c02972.